Geophys. J. Int. (2009) **179,** 929–944 doi: 10.1111/j.1365-246X.2009.04345.x

Imaging Earth's crustal magnetic field with satellite data: a regularized spherical triangle tessellation approach

Reto Stockmann, Christopher C. Finlay and Andrew Jackson

Institute of Geophysics, ETH Zurich, Switzerland. E-mail: cfinlay@erdw.ethz.ch

Accepted 2009 July 24. Received 2009 June 23; in original form 2009 March 20

SUMMARY

We present a method for imaging the global crustal magnetic field at Earth's surface using a local basis representation and a minimum norm model regularization approach. The local basis consists of a spherical triangle tessellation (STT) parametrization of the radial component of the crustal field at Earth's reference spherical surface. The Green's function for Laplace's equation in spherical geometry with Neumann boundary conditions provides the necessary forward modelling scheme. We solve the inverse problem of estimating the crustal field from satellite magnetic observations by minimizing an objective function comprising a mean absolute deviation (L_1-norm) measure of misfit plus a norm measuring model complexity. Both quadratic and entropy measures of field complexity are investigated. We report results from synthetic tests performed on a geophysically motivated scenario; these include a successful benchmark of the method and a comparison between quadratic and entropy regularization strategies. Applying our technique to real observations collected by the CHAMP, Ørsted and SAC-C satellites, we obtain stable images of the crustal magnetic field at Earth's surface that include sharp features with high amplitudes. We present details of two prototype crustal field models *STT-CRUST-Q* and *STT-CRUST-E* regularized using quadratic and entropy norms respectively; these provide a perspective complementary to that given by conventional spherical harmonic crustal field models.

Key words: Image processing; Inverse theory; Satellite magnetics.

1 INTRODUCTION

The terrestrial part of the Earth's magnetic field consists of a dominant core-generated field and a crustal magnetic field due to remanent and induced magnetization of constituent geological minerals. Maps of Earth's crustal (sometimes also referred to as lithospheric) magnetic field are useful in studies of crustal geology, thermal history and also regional tectonics (e.g. Langel & Hinze 1998; Purucker & Whaler 2007). Since 1999, satellites have continuously monitored Earth's magnetic field from space providing high quality data with a good and homogenous spatial coverage. Nevertheless, accurate retrieval of highly localized crustal field anomalies remains challenging because of the noisy nature of the observations, particularly at high latitudes where fields due to auroral electric currents contaminate the signal, and because of the blurring introduced by the hundreds of kilometres distance between the satellites and the sources at Earth's surface. In this paper, we introduce a new method for robustly estimating the global crustal magnetic field at Earth's surface. We adopt a spherical triangle tessellation (STT) basis (Constable *et al.* 1993) rather than the conventional spherical harmonic (SH) model parametrization. The STT basis has the advantage of local support—the value of the field at any location is dependent on at most three model coefficients (the adjacent nodes of the grid) in contrast to the situation with a SH basis where it depends on the entire set of model parameters. Such a local basis is arguably better suited for modelling the localized field anomalies that characterize the crustal field. We also search for crustal field models that adequately fit the observations but are characterized by the minimal required spatial complexity. We explore both conventional quadratic regularization (Tikhonov & Arsenin 1977; Gubbins 1983; Whaler 1994) and the more sophisticated technique of maximum entropy regularization (Gull & Daniell 1978; Gull & Skilling 1984; Jackson *et al.* 2007a) which was developed for image reconstruction problems requiring the retrieval by deconvolution of sharp features from noisy and incomplete observations.

Of course, many previous studies have been carried out in which crustal magnetic fields have been inferred from satellite magnetic measurements. The first global scale images of Earth's crustal magnetic field were derived in the mid-1970s from POGO scalar field data (Regan *et al.* 1975). Following the MAGSAT mission a number of more detailed maps were produced (Cain *et al.* 1989; Cohen & Achache 1990; Arkani-Hamed *et al.* 1994; Ravat *et al.* 1995). Unfortunately, these were all limited by the rather small amount of MAGSAT data, inaccuracies in the intensity only POGO data and difficulties in accounting for external fields. The past five years have seen a dramatic leap forward in the fidelity of crustal magnetic field

© 2009 The Authors
Journal compilation © 2009 RAS

models driven by the abundance high accuracy, magnetically quiet data delivered by the low Earth orbit satellites CHAMP, Ørsted and SAC-C.

Two strategies have dominated recent attempts to construct models of the crustal field from this new satellite data. Both are based on a global spherical harmonic model parametrization, but they involve rather different strategies for data treatment. Maus *et al*. in the *MF* series of models have adopted a dedicated, sequential, crustal field modelling approach in which the data are deterministically corrected and filtered to remove the influence of core, magnetospheric, tidal and other field sources as best as possible before an inversion is performed for the crustal field alone (Maus *et al.* 2002, 2006b, 2007b, 2008). A discussion of the philosophy underlying this approach and results of tests carried out using synthetic data are given by Maus *et al.* (2006a). The most recent model in this series is the *MF6* model which it's authors claim is reliable up to spherical harmonic degree 120; a spectacular success of this model is the ability to resolve the direction of magnetic remanence patterns which appear as stripes parallel to oceanic spreading centres.

The other main approach pursued has been to simultaneously co-estimate the internal (core and crustal) field, along with various components of the external field. Then, after the inversion, the crustal field model is isolated from the core field model by selecting spherical harmonic degrees of the static internal field greater than 15. Analysis of the spatial spectrum suggests that below this point the core field dominates while above it the crustal field is stronger due to geometrical attenuation of the short wavelength signal from the core. Models constructed from recent satellite and observatory data following this strategy include the 'Comprehensive Model' series by Langel *et al.* (1996) and Sabaka *et al.* (2002, 2004), the *CHAOS* series by Olsen *et al.* (2006a) and Olsen & Mandea (2008), the models developed by Thomson & Lesur (2007), and the *GRIMM* model produced by Lesur *et al.* (2008). Although these models are based on data sets selected using different criteria and involve rather different parametrizations of the external field they now agree rather well on the large scale crustal magnetic field up to spherical harmonic degree 45 (Lesur *et al.* 2008). Systematic differences between these models and the *MF* series of models have been reported at degrees 15–45; it has been suggested that these are related to the along track filtering method applied in construction of the *MF* models (Sabaka *et al.* 2004; Lesur *et al.* 2008). At shorter wavelengths (above spherical harmonic degree 45) there is still no consensus between the various models and the problem of determining which crustal field features are robust remains a major challenge.

As noted by O'Brien & Parker (1994), the spherical harmonic basis (adopted by all the studies discussed above) is unfortunately rather ill-suited for crustal field modelling. This is fundamentally because of the localized nature of the geological sources compared to the global sensitivity of spherical harmonics; an enlightening discussion of this issue in the context of global seismic tomography (where similar issues arise) has recently been given by Amirbekyan *et al.* (2008). A number of alternative local basis functions have consequently been explored. Methods involving the representation of the crustal field by a grid of equivalent dipole sources have been developed by Mayhew (1979) and extended by Covington (1993) to an icosahedral grid. This method has been employed by Purucker *et al.* (1996) to produce models of the crustal field of Earth, Mars (Langlais *et al.* 2004) and the moon (Purucker 2008); it has also proved to be useful in constructing crustal magnetization models. O'Brien & Parker (1994) proposed a local basis consisting of a grid of magnetic monopoles; they demonstrated that this could be used for both global and local field modelling. Following the suggestion by Shure *et al.* (1982) and Parker & Shure (1982), Whaler (1994) and Langel & Whaler (1996) have developed models on a (depleted) harmonic spline basis and have applied this method to Earth and to Mars (Whaler & Purucker 2005). One may ask why these local techniques have not become more widely adopted for high resolution modelling of Earth's global crustal magnetic field from satellite data. The difficulty seems to be that spherical harmonics are attractive because they arise in a natural way in the analytic solution of Laplace's equation in spherical geometry, and because the local methods are generally more difficult to code and can be computationally more expensive, for example requiring conjugate gradient optimization routines in order to solve the resulting large matrix systems (Purucker *et al.* 1996). An additional drawback of the local modelling approach is the difficulty in suppressing spurious north–south trending stripes that can be mapped into crustal field models due to along track spatially correlated noise. As described in Section 2 and demonstrated in the results presented in Section 4, the regularized STT method presented in this study permits high resolution global, stable, models to be obtained in a straightforward and efficient manner using a standard quasi-Newton optimization scheme.

An alternative approach to obtaining local basis functions on a spherical surface involves modifying spherical harmonics so they give support only over a limited region, for example in the method of spherical cap analysis (Haines 1985; De Santis *et al.* 1999) and its revisions (Thébault *et al.* 2006a,b; Thébault 2008). The most advanced application of this approach to the problem of global crustal field modelling from satellite data has been described by Thébault (2006). Lesur (2006) proposed another elegant approach whereby quasi-localized functions with well-defined spherical harmonic content can be constructed; Lesur & Maus (2006) used this method to obtain a crustal field model with locally restricted spectral content in the troublesome polar regions. Simons *et al.* (2006) and Simons & Dahlen (2006) have also recently developed a promising strategy involving band-limited spherical functions whose energy is optimally concentrated in a geographically localized region; this method has however not yet been applied in crustal field modelling. It should further be noted that Freeden *et al.* (1998) and Freeden & Schreiner (2009) have developed sophisticated mathematical tools (based on vector kernel functions) that allow one to work in a local but multi-resolution basis in spherical geometry. Their approach was applied in geomagnetism to the internal–external field separation problem by Mayer & Meier (2006), but it has not yet been used for crustal field modelling. Many of the methods discussed in this paragraph approach the spherical harmonics when the domain of interest becomes global—in this case they lose their attractive local character. If instead one restricts them to some local region then a series of difficult mergers are required (see, for example, Thébault 2006). The STT basis used in the present study is by contrast truly local, while also being specifically designed to represent potential fields everywhere on a spherical surface, and avoiding any problems at the poles. As described by Constable *et al.* (1993) it involves an icosahedral discretization of the two-sphere into spherical triangles (Baumgardner & Frederickson 1985). These define a continuous (but not infinitely differentiable), piecewise linear basis that is the 2-D equivalent on a spherical surface of a 1-D basis involving B-splines of order 2 (Jackson *et al.* 2007b). Further mathematical details concerning the implementation of the STT basis are given in Section 2.

To obtain a model of the crustal magnetic field at Earth's surface from satellite observations made at altitudes of 300–800 km requires

downward continuation of a potential field. This procedure is well known to be unstable in the presence of poorly determined model parameters. Two solutions to this problem that have previously been explored are: (i) truncation of the model to retain only the spatial scales which are believed to be well determined (see, e.g. Olsen *et al.* 2006b; Lesur *et al.* 2008; Maus *et al.* 2008) and (ii) regularization during model construction so that the models obtained are stable and well converged at the surface of interest (see, e.g. Whaler 1994; Maus *et al.* 2006b). The regularization or minimum norm approach (Tikhonov & Arsenin 1977; Parker 1994; Gubbins 2004) has been widely used for the past 25 years to construct trustworthy models of the core magnetic field at the core–mantle boundary (Shure *et al.* 1982; Gubbins & Bloxham 1985)—a classic example of solving an unstable downward continuation problem in geomagnetism. The approach is philosophically attractive because the non-uniqueness inherent in the inverse problem is mitigated by searching for a model which minimizes a chosen measure of field complexity, in addition to fitting the observations to within error estimates. We argue here that a minimum norm approach to the crustal field determination problem can provide a useful perspective on those field structures that can be unambiguously determined from recent satellite data.

In the small number of previous applications of regularization in crustal field modelling, simple quadratic measures of field complexity such as the square of vertical field (Z) integrated over the Earth's surface (Whaler 1994), or *ad hoc* penalization of unstable model coefficients (Maus *et al.* 2006b) were employed. *Ad hoc* regularization of specific coefficients makes it difficult to state precisely what measure of model complexity is minimized and leaves open the possibility that not all parts of the resulting image are stable at Earth's surface, so we prefer not to follow this path. Instead here we use the techniques described in Section 2 to first construct models which, similar to the work of Whaler (1994), minimize the square of radial field integrated over Earth's surface. This procedure permits stable, low complexity field models to be constructed at Earth's surface, but unfortunately also tends to artificially depress the crustal field amplitude and prevents sharp local features from being accurately imaged. We therefore also construct models regularized using a well-known non-quadratic measure of complexity, namely entropy. We use the term entropy in the information-theory sense (Shannon 1948; Jaynes 1957) and adopt a definition which satisfies the properties of subset independence, coordinate invariance, system independence and scaling (Skilling 1988) and is appropriate for non-positive functions (Gull & Skilling 1990; Hobson & Lasenby 1998)—further details are given in Section 2. Construction of models which maximize entropy while remaining consistent with observations has proven to be a very successful strategy in a wide variety of other image deconvolution problems, especially where retrieval of objects with high dynamic range from noisy and incomplete data is desired (see, e.g. Buck & Maculay (1991) or Sivia & Skilling (2006), chapter 6).

In Section 4.2, we report results of a geophysically motivated synthetic test where both the target crustal field and statistics of the contaminating noise are perfectly known; the synthetic data set is described in Section 3.2. We compare the merits of quadratic and maximum entropy regularization in this well-controlled scenario and find that the maximum entropy method is capable of producing images with greater contrast, and possessing better localized structures. Prototype models derived from real satellite observations using both quadratic and entropy regularization inversion methods are reported in Section 4.3. The purpose of presenting these models is to demonstrate the utility of our new modelling scheme–our focus here is not on how best to process and filter the satellite observations and issues such as anisotropy or space–time dependence of error budgets are not considered. The details of the satellite data selection and processing are given in Section 3.1. A discussion of the results obtained, comparison to some other crustal field models and possible future extensions of the method are given in Section 5 before conclusions are presented in Section 6.

2 METHODOLOGY

2.1 Crustal magnetic field representation

We adopt the spherical polar coordinate system and denote position by $\mathbf{r} = (r, \theta, \phi)$ where r is radius, θ is co-latitude and ϕ is longitude. In what follows we assume that the crustal field is to a good approximation static and ignore its time variation (for a justification see Thébault *et al.* 2009). We construct a model of the crustal magnetic field at the reference radius of the Earth's surface ($a = 6371.2$ km) and use this to account for the static short wavelength magnetic field measured by satellites. The atmosphere is approximated as an insulator where no electric currents flow so the magnetic field $\mathbf{B}$ due to crustal sources is assumed to be a potential field and represented by

$$\mathbf{B} = -\nabla V, \tag{1}$$

where V is the magnetic potential. Since $\nabla \cdot \mathbf{B} = 0$, V satisfies Laplace's equation

$$\nabla^2 V = 0. \tag{2}$$

The solution for the potential V accounting only for internal sources, is conventionally written in terms of a spherical harmonic expansion

$$V = a \sum_{l=1}^{\infty} \sum_{m=0}^{l} \left(\frac{a}{r}\right)^{l+1} \left[g_l^m \cos m\phi + h_l^m \sin m\phi\right] P_l^m(\cos\theta), \tag{3}$$

where g_l^m, h_l^m are the Gauss coefficients and P_l^m are the Associated Legendre Functions.

Here we explore an alternative approach where the field is instead parametrized directly in physical space in terms of the radial magnetic field B_r at $r = a$ and evaluated for $r > a$ using appropriate Green's functions (Gubbins & Roberts 1983). Constable *et al.* (1993) have presented the mechanics of this approach when modelling the geomagnetic field at Earth's core surface; the same apparatus largely carries over to modelling the crustal field at Earth's surface so the following account closely resembles their treatment.

Defining an appropriate Green's function, $G(\mathbf{r}, \hat{\mathbf{s}})$, where $\hat{\mathbf{s}}$ is a unit vector ranging over the surface S, and denoting the radial field on the Earth's surface S by $B_r(\hat{\mathbf{s}})$, then the magnetic potential $V(\mathbf{r})$ at any point outside S with $r > a$ may be written as

$$V(\mathbf{r}) = \int_S G(\mathbf{r}, \hat{\mathbf{s}}) B_r(\hat{\mathbf{s}})\, d^2\hat{s}. \tag{4}$$

This approach is justified by the existence theorem for the solution of the exterior Neumann boundary value problem for Laplace's equation (see, for example, Kellogg 1954, chapter 9, p. 246). The components of the gradient of this Green's function in spherical polar coordinates required to calculate the observed northward, eastward and downward vector magnetic field components (X, Y, Z) may then be written in the form

$$G_X(\mathbf{r}) = \frac{1}{r}\frac{\partial G}{\partial \theta} = \frac{1}{4\pi R^3}\left\{\frac{1 + 2R - \rho^2}{T}\right\} \rho^3 \hat{\mathbf{s}} \cdot \hat{\boldsymbol{\theta}}, \tag{5}$$

$$G_Y(\mathbf{r}) = -\frac{1}{r\sin\theta}\frac{\partial G}{\partial \phi} = -\frac{1}{4\pi R^3}\left\{\frac{1 + 2R - \rho^2}{T}\right\} \rho^3 \hat{\mathbf{s}} \cdot \hat{\boldsymbol{\phi}}, \tag{6}$$

© 2009 The Authors, *GJI*, **179,** 929–944
Journal compilation © 2009 RAS

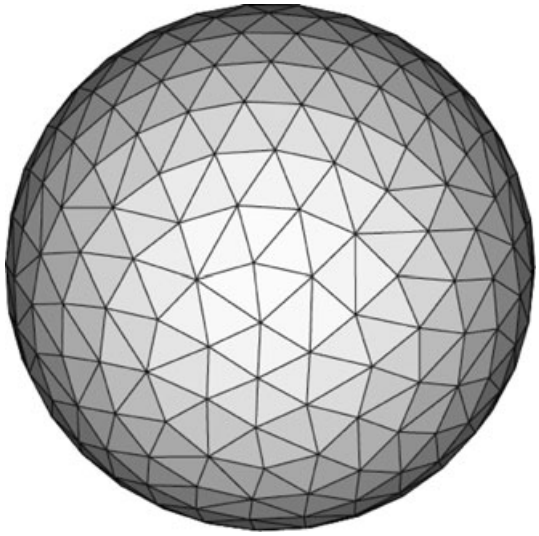

Figure 1. A tessellation of the sphere by spherical triangles, generated by bisections and trisections of the regular icosahedron on the unit sphere, following Baumgardner & Frederickson (1985). Here the nodes are joined by straight lines, generating planar surfaces; in our calculations we join the nodes by great circles, generating spherical triangles.

$$G_Z(\mathbf{r}) = \frac{\partial G}{\partial r} = -\frac{1}{4\pi}\left\{\frac{\rho^2(1-\rho^2)}{R^3} - \rho^2\right\}, \tag{7}$$

where $\rho = a/r$, $\mu = \hat{\mathbf{r}} \cdot \hat{\mathbf{s}}$, $R = \sqrt{1 - 2\mu\rho + \rho^2}$ and $T = 1 + R - \mu\rho$. $\hat{\mathbf{r}}$ is the unit vector in the direction of the observation location. The local directions at the observation location pointing southward and eastward, respectively are denoted by $\hat{\boldsymbol{\theta}}$ and $\hat{\boldsymbol{\phi}}$. Further details concerning the derivation of these Green's functions are found in the appendix of Constable *et al.* (1993).

In order to represent $B_r(\hat{\mathbf{s}})$ in a discrete fashion we once more follow Constable *et al.* (1993) and adopt a local spherical triangle tessellation (STT) basis (Baumgardner & Frederickson 1985) rather than the traditional truncated spherical harmonic global basis. In the STT approach $B_r(\hat{\mathbf{s}})$ is represented by a finite set of M nodes; as demonstrated by Baumgardner & Frederickson (1985) these define $2M - 4$ spherical triangles on the sphere of unit radius as illustrated in Fig. 1. Note that the edges of the spherical triangles are defined by geodesic arcs so there is no geometrical distortion associated with using this grid in a spherical geometry. At positions intermediate between the nodes, the field is calculated by linear interpolation of B_r within the gnomonic projection of each spherical triangle onto a plane tangent at its centroid. Under this parametrization the value and sign of the field at any point on s is dependent on at most three node values whereas with a spherical harmonic representation the point value depends on the weighted sum of the entire set of model parameters. For each node in the STT model an index is assigned; the tessellation is then specified by a list of triplets forming the vertices of each triangle (Baumgardner & Frederickson 1985). With this discretization the integrals required to compute the commonly measured northward, eastward and vertically downwards geomagnetic field components $(X, Y, Z) = (-B_\theta, B_\phi, -B_r)$ are reduced to simple numerical summations over the spherical triangles so that

$$X(\mathbf{r}) = \sum_{i=1}^{2M-4} \int_{\Delta_i} G_X\, B_r(\hat{\mathbf{s}})\, d^2\hat{s}, \tag{8}$$

$$Y(\mathbf{r}) = \sum_{i=1}^{2M-4} \int_{\Delta_i} G_Y\, B_r(\hat{\mathbf{s}})\, d^2\hat{s}, \tag{9}$$

$$Z(\mathbf{r}) = \sum_{i=1}^{2M-4} \int_{\Delta_i} G_Z\, B_r(\hat{\mathbf{s}})\, d^2\hat{s}, \tag{10}$$

where Δ_i stands for the ith spherical triangle. The integral over each spherical triangle is performed numerically. Two additional comments are worth making concerning this STT field representation. First, as discussed by Jackson *et al.* (2007b), the STT representation does not explicitly require the no monopole condition to be obeyed. Nonetheless, in the STT models we present here, the diagnostic ratio calculated directly in the STT domain $\int_S B_r d^2\hat{s}/(\int_S Br^2 d^2\hat{s})^{1/2} < 0.01$, while the $l = 0$ term obtained by spherical harmonic transform $|g_0^0| < 0.03$ nT, so the contribution of the monopole term is insignificant. We note that the divergence free constraint could be explicitly imposed if desired, at very little extra computational cost. Second, because the STT representation involves linear interpolation between nodes it is only piecewise linear continuous and not infinitely differentiable in contrast to spherical harmonics. This unfortunately makes exact transformations from STT models to spherical harmonics models impossible. However, this restriction is irrelevant to the production of accurate and useful images of the crustal field, provided the grid parametrization is sufficiently fine as is the case here.

2.2 The crustal field modelling forward problem

In the crustal field modelling problem, we compare the predicted vector components of the crustal field (X, Y, Z) with the observed vector field minus the vector field components predicted by a chosen core field model. In practice, it is also necessary to deal with scalar field (intensity) anomaly observations especially at high latitudes where vector satellite data is difficult to use. If we assume that the observed field $\mathbf{B}_{\text{obs}}$ (after correction for external fields) consists only of contributions from the core and crustal field then the scalar intensity of the observed field is

$$|\mathbf{B}_{\text{obs}}| = \sqrt{(\mathbf{B}_{\text{core}} + \mathbf{B})^2}, \tag{11}$$

where $\mathbf{B}_{\text{core}}$ is the core field and $\mathbf{B} = (X, Y, Z)$ is as before the field due to crustal magnetization. Since $|\mathbf{B}| \ll |\mathbf{B}_{\text{core}}|$ then to a good approximation, as shown in Blakely (1995) and Langel & Hinze (1998),

$$|\mathbf{B}_{\text{obs}}| \approx |\mathbf{B}_{\text{core}}| + \frac{\mathbf{B}_{\text{core}} \cdot \mathbf{B}}{|\mathbf{B}_{\text{core}}|}. \tag{12}$$

The scalar (intensity) anomaly due to the crustal field

$$\Delta F = |\mathbf{B}_{\text{obs}}| - |\mathbf{B}_{\text{core}}|, \tag{13}$$

may therefore be approximated by substituting from (12)

$$\Delta F \approx \frac{\mathbf{B}_{\text{core}} \cdot \mathbf{B}}{|\mathbf{B}_{\text{core}}|}. \tag{14}$$

This scalar anomaly ΔF is found from the observed intensity F by subtracting the intensity predicted by a core field model. Under approximation (14), ΔF is then linearly related to the vector components of the crustal field (X, Y, Z) as defined in eqs (8) to (10). Langel & Whaler (1996) demonstrated that this linear approximation involved an error much smaller than possible observation

errors. This linearized treatment of the scalar data greatly simplifies the inverse problem discussed below.

The resulting linear forward problem of predicting the vector components or intensity anomaly at a particular observation location from a known model of the crustal field $B_r(\hat{\mathbf{s}})$ at Earth's reference surface can be written in discrete form as

$$\tilde{\mathbf{d}} = \mathbf{A}\mathbf{m}, \tag{15}$$

where elements of vector $\tilde{\mathbf{d}}$ are the predicted field elements, $\mathbf{m}$ are the model parameters, that is, the crustal magnetic field at the M nodes, $m_i = (B_r)_i$, and $\mathbf{A}$ is a matrix of the forward functionals relating the model $\mathbf{m}$ to $\tilde{\mathbf{d}}$ as described in eqs (8) to (10) and (14). Model predictions for observed vector field components X, Y, Z and the scalar field anomaly ΔF can thus easily be calculated from a given crustal field model $\mathbf{m}$ together with an assumed core field model.

Due to the imperfect measurements and the incomplete model, real observations $\mathbf{d}$ and predictions of the forward model are not exactly equal, but are related by

$$\mathbf{d} = \mathbf{A}\mathbf{m} + \mathbf{e}, \tag{16}$$

where $\mathbf{e} = (\mathbf{d} - \tilde{\mathbf{d}})$ is an error vector of the residual between the observations $\mathbf{d}$ and the model predictions $\tilde{\mathbf{d}} = \mathbf{A}\mathbf{m}$.

2.3 The crustal field modelling inverse problem

Finding a crustal field model $\mathbf{m}$ consistent with observations of the crustal field $\mathbf{d}$ is an ill-posed problem: many possible models exist that could fit the data within their estimated errors (see, e.g. Parker 1994). One successful and widely used method of dealing with this difficulty is to regularize the inverse problem. When regularizing, one seeks the simplest model for a given fit to the data by searching for the $\mathbf{m}$ that minimizes not just the misfit between the data and the model predictions but also a norm measuring the model's complexity.

The conventional L_2-norm measure of misfit χ between the model predictions and the observations is given by

$$\chi = \sqrt{\frac{1}{N}\sum_{i=1}^{N}\left[\frac{d_i - \tilde{d}_i}{\sigma_i}\right]^2}, \tag{17}$$

where d_i is the ith observation, $\tilde{d}_i$ is the associated prediction from the forward model, σ_i is the estimated error of the datum and N is the number of observations. Model estimation methods based on L_2-norm measures of misfit certainly perform well when the noise that contaminates the signal of interest is truly random (Gaussian). However for non-Gaussian noise, as is expected when unmodelled fluctuations in external fields contaminate the observations, an L_1-norm (absolute deviation) measure of misfit has been shown in many studies to be a more robust method of model estimation (Claerbout & Muir 1971; Farquharson & Oldenburg 1998; Aster *et al.* 2005). The L_1-norm measure of misfit ξ takes the form

$$\xi = \frac{\sqrt{2}}{N}\sum_{i=1}^{N}\left|\frac{d_i - \tilde{d}_i}{\sigma_i}\right|. \tag{18}$$

Model estimation methods using the L_1-norm measure of misfit have recently been found to perform well in geomagnetic field modelling applications (Walker & Jackson 2000; Thomson & Lesur 2007; Lesur *et al.* 2008). The L_1-norm approach enables robust crustal field models to be obtained even at high-latitudes where there is large amplitude noise due to electrical currents flowing in the auroral region. We implement the L_1-norm using an iteratively reweighted least squares (IRWLS) algorithm (Scales *et al.* 1998; Walker & Jackson 2000). This procedure is started from an initial inversion produced using the conventional L_2-norm method.

To implement the L_1-norm we modify the standard regularized least squares problem (Gubbins 2004; Aster *et al.* 2005) to an optimization problem to find the model $\mathbf{m}$ which minimizes the objective function

$$\Theta(\mathbf{m}) = [\mathbf{d} - \mathbf{A}\mathbf{m}]^T \mathbf{C}_e^{-1/2}\mathbf{W}_k\mathbf{C}_e^{-1/2}[\mathbf{d} - \mathbf{A}\mathbf{m}] + \lambda\mathbf{R}(\mathbf{m}), \tag{19}$$

where $\mathbf{W}_k$ is a weighting matrix derived from the misfit of each datum in the previous (kth) model iteration (Walker & Jackson 2000), $\mathbf{C}_e$ is the data covariance matrix containing information concerning estimated errors, λ is a constant known as the damping parameter and $\mathbf{R}(\mathbf{m})$ is the regularization norm. The first (misfit) term measures the difference between model predictions and the observations weighted by the estimated observation errors. The second (regularization) term is a norm measuring the model complexity. The damping parameter λ controls the relative importance of fit to the data and model complexity.

If $\mathbf{R(m)}$ is non-quadratic then minimizing (19) is a non-linear optimization problem requiring an iterative approach for its solution. Here, we use a quasi-Newton scheme (see, e.g. Luenberger 1969; Tarantola 2005). This may be written in the form

$$\mathbf{m}_{k+1} = \mathbf{m}_k - \mu_k\left[\nabla\nabla\Theta(\mathbf{m}_k)\right]^{-1}\left[\nabla\Theta(\mathbf{m}_k)\right], \tag{20}$$

where μ_k are real constants small enough to avoid divergence of the algorithm and large enough to allow the algorithm to advance. μ_k are here chosen to be unity, since the Hessian metric accounts sufficiently well for the local geometry of the objective function. Substituting (19) into (20) and taking $\mu_k = 1$ leads to the scheme

$$\begin{aligned}\mathbf{m}_{k+1} = \mathbf{m}_k &+ \left[2\mathbf{A}^T\mathbf{C}_e^{-1/2}\mathbf{W}_k\mathbf{C}_e^{-1/2}\mathbf{A} + \lambda\nabla\nabla\mathbf{R}(\mathbf{m}_k)\right]^{-1} \\ &\times\left[2\mathbf{A}^T\mathbf{C}_e^{-1/2}\mathbf{W}_k\mathbf{C}_e^{-1/2}(\mathbf{d} - \mathbf{A}\mathbf{m}_k) - \lambda\nabla\mathbf{R}(\mathbf{m}_k)\right].\end{aligned} \tag{21}$$

Following Jackson *et al.* (2007b) and using a variant of the quasi-Newton algorithm that solves for the $\mathbf{m}_{k+1}$, rather than a perturbation $\delta\mathbf{m}$ to $\mathbf{m}_k$, the iterative scheme becomes

$$\begin{aligned}\mathbf{m}_{k+1} = &\left[2\mathbf{A}^T\mathbf{C}_e^{-1/2}\mathbf{W}_k\mathbf{C}_e^{-1/2}\mathbf{A} + \lambda\nabla\nabla\mathbf{R}(\mathbf{m}_k)\right]^{-1} \\ &\times\left[2\mathbf{A}^T\mathbf{C}_e^{-1/2}\mathbf{W}_k\mathbf{C}_e^{-1/2}\mathbf{d} + \lambda\nabla\nabla\mathbf{R}(\mathbf{m}_k)\mathbf{m}_k - \lambda\nabla\mathbf{R}(\mathbf{m}_k)\right].\end{aligned} \tag{22}$$

Note that when $\mathbf{W}_k = \mathbf{I}$, where $\mathbf{I}$ is the identity matrix, this scheme reduces to that for the conventional regularized least-squares problem. Iteration is required to find a solution because $\mathbf{W}_k$ depends on $\mathbf{m}_k$.

In this study, we explore both a conventional quadratic regularization norm (Shure *et al.* 1982; Gubbins & Bloxham 1985; Whaler 1994) and also an entropy regularization norm which is a non-quadratic measure of complexity (Gull & Daniell 1978; Jackson *et al.* 2007a). In the next two sub-sections we discuss the mathematical form of these choices of regularization in detail.

2.3.1 *Quadratic regularization*

We perform quadratic regularization using the integral of the square of the radial component of the crustal magnetic field over Earth's surface

$$\int_S B_r^2 \, d^2\hat{s}. \tag{23}$$

© 2009 The Authors, *GJI*, **179,** 929–944
Journal compilation © 2009 RAS

Following Constable *et al.* (1993), an approximation to this norm using a SST basis summing over the $2M - 4$ spherical triangles takes the form

$$\mathbf{R}_Q(\mathbf{m}) = \sum_i^{2M-4} (B_r)_i^2. \tag{24}$$

The appropriate gradient and the Hessian operators required in the quasi-Newton algorithm are therefore

$$(\nabla \mathbf{R}_Q)_i = 2m_i, \tag{25}$$

$$(\nabla\nabla \mathbf{R}_Q)_{ij} = \nabla(2m_i)_j = 2\delta_{ij}, \tag{26}$$

where δ_{ij} is the Kronecker delta.

The iterative scheme (22) for this choice of quadratic regularization therefore takes the form

$$\mathbf{m}_{k+1} = \left[\mathbf{A}^T\mathbf{C}_e^{-1/2}\mathbf{W}_k\mathbf{C}_e^{-1/2}\mathbf{A} + \lambda\mathbf{I}\right]^{-1}\left[\mathbf{A}^T\mathbf{C}_e^{-1/2}\mathbf{W}_k\mathbf{C}_e^{-1/2}\mathbf{d}\right]. \tag{27}$$

2.3.2 Maximum entropy regularization

Use of an entropy norm for regularization (often referred to as the maximum entropy method) has been employed by many workers in a diverse range of applications in the past 20 years (Gull & Daniell 1978; Gull & Skilling 1984; Sivia & Skilling 2006). We refer readers to Jackson *et al.* (2007a) for details of the calculation of the entropy of a magnetic field on a spherical surface discretized using an STT basis. To facilitate comparisons with quadratic regularization we follow Gillet *et al.* (2007) and use the following form of the negentropy as a measure of field complexity,

$$S[\mathbf{m}, w] = -4w\sum_{i=1}^{M}\left\{\psi_i - 2w - m_i\log\left[\frac{\psi_i + m_i}{2w}\right]\right\}. \tag{28}$$

Here w is the default parameter and $\psi_i = \sqrt{m_i^2 + 4w^2}$. This form assumes that the default parameter takes the same value for each node. The default parameter w specifies the width of the entropy function (Maisinger *et al.* 2004); it should ideally be set using prior knowledge concerning the expected magnitude of the unsigned flux $\int_S |B_r| d^2\hat{s}$ of the crustal field. However, in the absence of definitive prior knowledge it can be treated as a free parameter and varied to obtain suitably sharp images (Jackson *et al.* 2007a). Defining the above expression for the negentropy of the image to be a regularization norm (i.e. $\mathbf{R}_S = S[\mathbf{m}, w]$), the required gradient and Hessian operators are

$$\begin{aligned}(\nabla\mathbf{R}_S)_i &= (\nabla S)_i \\ &= -4w\left\{\frac{m_i}{\psi_i} - \log\left[\frac{\psi_i + m_i}{2w}\right] - \frac{m_i}{\psi_i + m_i}\left(\frac{m_i}{\psi_i} + 1\right)\right\} \\ &= 4w\log\left[\frac{\psi_i + m_i}{2w}\right],\end{aligned} \tag{29}$$

and

$$(\nabla\nabla\mathbf{R}_S)_{ij} = (\nabla\nabla S)_{ij} = \frac{4w}{\psi_i + m_i}\left(\frac{m_i}{\psi_i} + 1\right)\delta_{ij} = \frac{4w}{\psi_i}\delta_{ij}, \tag{30}$$

where δ_{ij} is again the Kronecker delta. Our iterative optimization scheme for the maximum entropy regularization is then

$$\begin{aligned}\mathbf{m}_{k+1} &= \left[2\mathbf{A}^T\mathbf{C}_e^{-1/2}\mathbf{W}_k\mathbf{C}_e^{-1/2}\mathbf{A} + \lambda\boldsymbol{\alpha}_k\right]^{-1} \\ &\quad\times\left[2\mathbf{A}^T\mathbf{C}_e^{-1/2}\mathbf{W}_k\mathbf{C}_e^{-1/2}\mathbf{d} + \lambda\boldsymbol{\alpha}_k\mathbf{m}_k - 4w\lambda\boldsymbol{\beta}_k\right],\end{aligned} \tag{31}$$

with

$$\boldsymbol{\alpha}_k = \mathrm{diag}\left\{\frac{4w}{\psi_1}, \frac{4w}{\psi_2}, \ldots, \frac{4w}{\psi_M}\right\},$$

$$\boldsymbol{\beta}_k = \left\{\log\left(\frac{\psi_1 + m_1}{2w}\right), \log\left(\frac{\psi_2 + m_2}{2w}\right), \ldots, \log\left(\frac{\psi_M + m_M}{2w}\right)\right\}.$$

[Correction made after online publication 14 September 2009: in the second line of equation (31), the term '$\mathbf{m}_k$' has been inserted after '$\lambda\boldsymbol{\alpha}_k$'].

In the next section, we describe the satellite data set used to demonstrate the operation of the STT-regularized crustal field modelling scheme described above, and a synthetic data set used to test its performance in a controlled scenario.

3 DATA COMPILATION

3.1 Satellite data for crustal field modelling

We employ a well established, high quality, satellite data set to test our new modelling procedure in order to permit a straightforward comparison to previous results. This is the *xCHAOS_03p_08* data set selected and previously used by Olsen & Mandea (2008) to derive their *xCHAOS* model. It consists of more than 8.5 yr of CHAMP, Ørsted and SAC-C geomagnetic satellite data with Ørsted scalar and vector data between 1999 March and 2007 December, CHAMP scalar and vector data between 2000 August and 2007 December and SAC-C scalar data between 2001 January and 2004 December. The selection of geomagnetically quiet data for the *xCHAOS* data set followed the same protocol as for the *CHAOS* data set of Olsen *et al.* (2006a): (i) at all latitudes the D_{st}-index must change by less than 2 nT hr^{-1}; (ii) at non-polar latitudes (equatorwards of 60° geomagnetic dipole latitude) it is required that $Kp \leq 2o$; (iii) for regions polewards of 60° geomagnetic latitude the merging electric field at the magnetopause must be less than 0.8 mVm^{-1}; (iv) only data from dark regions (sun 10° below horizon) were used; (v) vector data were accepted for geomagnetic dipole latitudes equatorwards of ± 60° while only scalar data were used for regions polewards of ±60° or if attitude data were not available and (vi) non-polar CHAMP data are used only after local midnight, to avoid the influence of the diamagnetic effect of dense plasmas. This selection criteria has in the past successful enabled the construction of high resolution models of both the core and crustal magnetic field.

From the observations in the *xCHAOS_03p_08* data set we subtracted the *xCHAOS* model predictions for the external (magnetospheric) field and for the core field and its secular variation up to spherical harmonic degree 14. We refer to this set of corrected observations as *xCHAOS-corr* : they are observations of the magnetic signal due to crustal magnetization of interest, but also contain unwanted contaminating signals from ionospheric electrical currents, tidal and steady current driven induction in the oceans; induction in the 3-D conducting mantle, lithosphere and oceans driven by external electric currents, measurement errors, and errors due to imperfections in the core and magnetospheric models that were subtracted. To obtain a spatially homogeneous, magnetically quiet, data set we further decimated *xCHAOS-corr* retaining a subset filling as well as possible a dense equal area grid consisting of 360 bins equally spaced in cosine latitude by 720 bins equally spaced in longitude. Within each bin we selected the datum that deviated least (in an absolute sense) from the *xCHAOS* prediction using the full model up to degree 50. Vector data from CHAMP were preferentially selected (due to their lower altitude), then vector data from Ørsted, then scalar data. For vector data the rms deviation of the

© 2009 The Authors, *GJI*, **179,** 929–944
Journal compilation © 2009 RAS

Table 1. Statistics of the satellite data set *xCHAOS-corr-sub* used in this study for crustal field estimation.

Data Source	Geomag. Lat. range	Comp.	N	Mean (nT)	rms (nT)	Error Est. (nT)
CHAMP	$\lvert mlat\rvert \leq 60^\circ$	X, Y, Z	348 396	0.01	3.82	3.5
	$\lvert mlat\rvert \leq 60^\circ$	F	1085	−0.44	3.89	3.5
	$\lvert mlat\rvert > 60^\circ$	F	11 545	−1.29	8.54	8.0
Ørsted	$\lvert mlat\rvert \leq 60^\circ$	X, Y, Z	150 705	−0.04	5.23	5.0
	$\lvert mlat\rvert \leq 60^\circ$	F	17 252	0.57	2.48	2.5
	$\lvert mlat\rvert > 60^\circ$	F	11 291	1.19	5.21	5.0
SAC-C	$\lvert mlat\rvert \leq 60^\circ$	F	10 342	0.11	3.07	2.5
	$\lvert mlat\rvert > 60^\circ$	F	6038	−0.04	5.17	5.0

Notes: The core field (up to degree 14) and magnetospheric field predicted by *xCHAOS* have been removed. *mlat* refers to the geomagnetic latitude in degrees. The number of data in each category, their mean and rms values in nT and estimated errors used in the inversions are reported in the final column.

three field components was used for selection. This procedure resulted in 556 655 data suitable for estimating the crustal magnetic field; we refer to this data set as *xCHAOS-corr-sub*. We acknowledge that our data selection criteria suffers from the problem that noise could in some cases fortuitously reduce the residual from the *xCHAOS* model with the result that the selected data might not be the least disturbed. Further investigation is needed concerning how best to combine data within a bin to produce unbiased field models. It could also be argued that when seeking to determine the crustal field it is be better to use only CHAMP data in which the crustal field signature is strongest and to use more quieter intensity data than we have chosen. For these reasons we refer to the models reported in Section 4.3 as prototypes. Though sufficient to demonstrate our modelling approach, they could undoubtedly be improved by a more sophisticated treatment of the data.

Table 1 summarises the statistics of the *xCHAOS-corr-sub* real data set, separated by satellite and field components. Note that the mean values of all the data subsets are fairly close to zero indicating that no large biases are present. The rms values for the Ørsted vector data are somewhat higher than those of the CHAMP vector data because the quietest low altitude CHAMP data are preferred during the selection process and because Ørsted vector data contain additional errors due to attitude uncertainty (Olsen 2002). The estimated errors we used to weight the data (through the covariance matrix $\mathbf{C}_e$) during inversions for field models are given in the final column of Table 1.

3.2 Synthetic data

To benchmark the inversion scheme described in Section 2, we first carried out tests using a synthetic data set. This is derived from a prior crustal magnetic field synthesized from the geology-based forward model of Hemant & Maus (2005) and the *NGDC-720* model (Maus 2006) which was one of the candidate models for the World Digital Magnetic Anomaly Map (Korhonen *et al.* 2007). The *NGDC-720* model of Maus (2006) is derived from marine, aeromagnetic and ground survey data (Maus *et al.* 2007a) together with a satellite field model (Maus *et al.* 2007b). The model of Hemant & Maus (2005) is used for spherical harmonic degrees 16–80 and the *NGDC-720* model of Maus (2006) is used for spherical harmonic degrees 81–140. We argue that the resulting model constitutes a geophysically plausible high resolution crustal magnetic field that can be used as a test of our inversion scheme. We transformed this synthetic spherical harmonic crustal field model onto a STT-grid with of 12 962 nodes. It is this STT model which is the synthetic reference 'truth' with which we compare the results of our test inversions.

We next constructed a data set that is as close as possible to the real satellite data set *xCHAOS-corr-sub* by evaluating the appropriate field components (vector or scalar) from the synthetic reference 'truth' model at the geographical positions (co-latitude, longitude and altitude) of the *xCHAOS-corr-sub* data. We refer to this noise-free data set as *xCHAOS-SYN-HMN_nf*—it was used to benchmark the inversion scheme as reported in Section 4.1. To this noise-free data set we added two independent noise sources. The first was designed to mimic noise due to unmodelled ionospheric auroral electrojet currents that we believe to be an important source of error, particularly in the CHAMP observations. It consists of random samples from a Laplacian probability density function (see, e.g. Walker & Jackson 2000) weighted by a spatial varying amplitude function with maximum amplitude at 110 km altitude in the auroral region. The amplitude scaling was chosen so its maximum value at 400 km altitude was 30 nT. In addition, a second source of random noise, this time drawn from a Gaussian probability density function, was added to account for additional noise sources specific to the vector and scalar measurements made by each satellite (see the rows of Table 2). The amplitude of this second noise source was chosen to bring the rms variability of each of these data subsets close to the estimated errors for the real data reported in Table 1. The statistics of the final synthetic data set *xCHAOS-SYN-HMN* used to

Table 2. Statistics of the synthetic data set *xCHAOS-SYN-HMN* used for the synthetic tests.

Data	Geomag. Lat. Range	Comp	N	Mean (nT)	rms (nT)	Error Est. (nT)
CHAMP	$\lvert mlat\rvert \leq 60^\circ$	X, Y, Z	348 396	0.00	3.80	3.5
	$\lvert mlat\rvert \leq 60^\circ$	F	1085	−0.06	3.84	3.5
	$\lvert mlat\rvert > 60^\circ$	F	11 545	0.02	8.51	8.0
Ørsted	$\lvert mlat\rvert \leq 60^\circ$	X, Y, Z	150 705	0.00	5.22	5.0
	$\lvert mlat\rvert \leq 60^\circ$	F	17 252	0.00	2.44	2.5
	$\lvert mlat\rvert > 60^\circ$	F	11 291	−0.11	5.17	5.0
$SAC-C$	$\lvert mlat\rvert \leq 60^\circ$	F	10 342	0.01	3.02	2.5
	$\lvert mlat\rvert > 60^\circ$	F	6038	−0.05	5.14	5.0

Note: The data have been separated into the same categories as the real satellite data set reported in Table 1.

© 2009 The Authors, *GJI*, **179,** 929–944
Journal compilation © 2009 RAS

obtain the inversion results reported in Section 4.2 are presented in Table 2.

4 RESULTS

4.1 Benchmark test with noise-free data

First, we report results of a simple test based on noise-free synthetic observations that constitutes a benchmark of our STT crustal field modelling method. The data set used for this test was the noise-free compilation *xCHAOS-SYN-HMN_nf* derived from the synthetic 'truth' crustal field model described in Section 3.2. For all the synthetic tests we used a STT grid with a refinement of $2 \times 2 \times 3 \times 3$ consisting of 12 962 nodes and 25 920 spherical triangles (or cells) with triangle sides of approximately 220 km. Note that the same STT grid was used in the construction of the synthetic 'truth' model. The benchmark involved performing an inversion using quadratic regularization with an extremely small damping parameter, $\lambda = 1 \times 10^{-7}$ (nT)$^{-2}$. We were able to almost perfectly reproduce the synthetic 'truth' obtaining a correlation coefficient of 1.0000 and a rms percentage difference between the retrieved field and the true field of 0.14 per cent; further quantitative details are presented in Tables 3 and 4. This successful benchmark shows that our STT crustal field modelling scheme functions correctly and illustrates that our data sets are sufficient to allow accurate field reconstruction of small scale field structures, assuming noise levels are sufficiently low.

4.2 Synthetic test: inversion for a known crustal field from noisy data

To test the performance of the method in more detail with noisy data and to compare the merits of quadratic and maximum entropy regularization a further suite of synthetic tests was carried out. These were based on the noisy synthetic data set *xCHAOS-SYN-HMN* described in Section 3.2 and also involve a STT model with 12 962 nodes and 25 920 spherical triangles.

The test inversions with the noisy data were carried out with the damping parameter $\lambda = 1 \times 10^{-3}$ (nT)$^{-2}$. This was found to correspond approximately to the knee of the trade-off (or L-curve) where misfit is plotted against model norm (e.g. Hansen 1998; Gubbins 2004; Aster *et al.* 2005). The trade-off curve was constructed from inversions using first an L_2-norm measure of misfit then further iterations with an L_1-norm measure of misfit. The number of iterations was limited by the computational expense, but the models were sufficiently converged to correctly establish the shape of the trade-off curve. The model with $\lambda = 1 \times 10^{-3}$ (nT)$^{-2}$ and using the quadratic norm for regularization is referred to as the 'quadratic' model in Tables 3, 4 and discussion below.

Starting with the 'quadratic' model a series of maximum entropy inversions (also derived using the L_1-norm measure of misfit), for a range of the default parameter w were carried out. We reiterate that the same damping parameter was employed for both the quadratic and maximum entropy regularized inversions. The level of misfit between all the entropy regularized models and the synthetic data set was very similar and close to 1, indicating, unsurprisingly, that our error estimates correctly quantified the level of noise we added

Table 3. Statistics of the inverted models derived from the synthetic data set *xCHAOS-SYN-HMN*.

Model	λ (nT)$^{-2}$	w (nT)	σ_{B_r} (nT)	min (B_r) (nT)	max (B_r) (nT)	misfit (L_1)
Truth ($L = 140$)	–	–	37.872	−801.035	446.608	1.092
Truth ($L = 60$)	–	–	16.094	−148.447	148.960	1.093
Benchmark	1×10^{-7}	–	37.873	−801.053	446.669	0.035
Quadratic	0.001	–	16.463	−168.196	133.814	1.087
Entropy	0.001	50.0	14.599	−190.029	140.181	1.088
	0.001	30.0	14.094	−233.941	158.274	1.088
	0.001	20.0	14.493	−264.804	171.305	1.088
	0.001	15.0	14.916	−285.014	183.480	1.087
	0.001	10.0	15.836	−359.102	225.160	1.087
	0.001	5.0	17.142	−382.002	246.146	1.087

Notes: λ is the preferred damping parameter and w the chosen default value. σ_{B_r} is the rms value of the B_r field amplitude at the models nodes. Min and max are the minimum and maximum node values of B_r, respectively. Misfit (L_1) stands for the L_1-norm measure of misfit of the model to the data, normalized by the error estimates.

Table 4. Statistics of the difference between the retrieved models from the synthetic data set *xCHAOS-SYN-HMN* and the 'truth' reference model ($L = 140$).

Model	λ (nT)$^{-2}$	w (nT)	σ^{diff} (nT)	ρ_{140}	ρ_{60}
Truth ($L = 140$)	–	–	0.000	1.0000	0.4260
Truth ($L = 60$)	–	–	16.094	0.4260	1.0000
Benchmark	1×10^{-7}	–	0.052	1.0000	0.4260
Quadratic	0.001	–	35.013	0.3845	0.7248
Entropy	0.001	50.0	34.909	0.3883	0.7778
	0.001	30.0	34.812	0.3944	0.7742
	0.001	20.0	34.772	0.3965	0.7677
	0.001	15.0	34.761	0.3969	0.7584
	0.001	10.0	34.715	0.4001	0.7381
	0.001	5.0	34.915	0.3921	0.6979

Notes: λ is the preferred damping parameter, w the chosen default value and σ^{diff} refers to the rms difference between the inverted and reference 'truth' ($L = 140$) models. ρ is the correlation coefficient of the inverted model to the reference 'truth' model truncated at spherical harmonic degree $L = 60$ and at full resolution ($L = 140$).

© 2009 The Authors, *GJI*, **179,** 929–944
Journal compilation © 2009 RAS

to the perfect synthetic observations. Statistics for the reference synthetic 'truth' model, a version of the 'truth' truncated at spherical harmonic degree $L = 60$, the 'quadratic' model and entropy models with the default parameter w varying between 50 and 5 nT are presented in Table 3.

To quantify the success of the inversions we use the following definition of the correlation coefficient in physical space, (see, e.g. Rice 1995, p. 132 and Langel & Hinze 1998, p. 79),

$$\rho = \frac{\sum_{i=1}^{M}(B_r)_i(B_r^{\mathrm{ref}})_i}{\sqrt{\sum_{i=1}^{M}(B_r)_i^2 \sum_{i=1}^{M}(B_r^{\mathrm{ref}})_i^2}}, \tag{32}$$

where $(B_r)_i$ and $(B_r^{\mathrm{ref}})_i$ are the radial magnetic field of the inverted model and the reference synthetic 'truth' model at the ith model node, respectively. We report ρ for the inverted models compared to the full reference 'truth' model up to spherical harmonic degree $L = 140$ (ρ_{140}) and to the same model truncated at degree $L = 60$ (ρ_{60}) together with the standard deviation of the rms differences between the inverted and full reference models (σ^{diff}) in Table 4. Fig. 2 shows Hammer–Aitoff projection plots of the radial component of the full ($L = 140$) reference 'truth' model (top) at Earth's surface in nT, the 'quadratic' regularized model (middle) and our preferred entropy regularized model with highest $\rho_{140}(w = 10$ nT) (bottom), also at Earth's surface in units of nT.

4.3 STT models of Earth's crustal magnetic field derived from real satellite data

In this section, we present results concerning two new STT based prototype models of the crustal magnetic field at Earth's reference spherical surface derived from the satellite data set *xCHAOS-corr-sub* described in Section 3.1. These models involve STT-grids with a refinement of $2 \times 2 \times 2 \times 2 \times 3$ consisting of 23 042 nodes and 46 080 spherical triangles (with approximate triangle sides of 1.5° or 170 km). Note however that it is the information content of the data and strength of the imposed regularization rather than the grid spacing that control the minimum lengthscale that can be imaged. These models were built in a similar manner to the models constructed with synthetic data described above. The damping parameter for both models was chosen to be $\lambda = 2.5 \times 10^{-4}$ (nT)$^{-2}$ which is close to the knee of the trade-off curve. The default parameter for the entropy inversions was also chosen to be $w = 10$ nT based on experience with the synthetic experiments (though we acknowledge that the noise level was somewhat higher in the synthetic tests compared to the real scenario and our reference 'truth' was not the real crustal field). An L_1-norm measure of misfit was employed and the models were iterated until satisfactory convergence was reached according to the criteria $\sqrt{\sum_{i=1}^{M}[(\mathbf{m}_k)_i - (\mathbf{m}_{k+1})_i]^2 / \sum_{i=1}^{M}[(\mathbf{m}_{k+1})_i]^2} < 10^{-2}$. Henceforth we refer to the quadratic model derived from the real data as *STT-CRUST-Q* and the preferred entropy model (with $w = 10$nT) derived from the real data as *STT-CRUST-E*.

In Fig. 3, we present plots of the radial magnetic field at Earth's surface in units of nT for *STT-CRUST-Q* (top panel) and *STT-CRUST-E* (bottom panel). To judge the quality of our models we compared them to a model that is thought to represent very well the large scale field [the *GRIMM* model for spherical harmonic degrees 15–45 (Lesur *et al.* 2008)—see Fig. 4 (top panel)] and also to a more ambitious model that claims to also represent smaller scale features [the *MF6* model for degrees 16–120 (Maus *et al.* 2008)—see Fig. 4 (bottom panel)]. The Lowes spectrum (Lowes 1974) showing the variance per degree at Earth's reference radius (up to degree 120) for *xCHAOS*, *MF6*, *GRIMM*, *STT-CRUST-Q* and *STT-CRUST-E* is presented in Fig. 5. Complementary information is given in Fig. 6 where the spherical harmonic degree correlation between our two STT-models and the three spherical harmonic models is presented. Note however that constructing these two figures required an imperfect transformation from the piecewise linear STT models to an infinitely differentiable spherical harmonic representation. Finally, a local comparison between *STT-CRUST-E* (middle panel), *GRIMM* (left-hand panel) and *MF6* model (right-hand panel) for North America is presented in Fig. 7.

Statistical information concerning *STT-CRUST-Q* and *STT-CRUST-E* together with similar details for *GRIMM*, *xCHAOS* and *MF6* are presented in Table 5. The misfit for both *STT-CRUST-Q* and *STT-CRUST-E* are less than 1.0. Since their damping parameters were chosen so they were close to the knee of the trade-off curve this indicates that our *a priori* error estimates reported in Table 1 were rather pessimistic. Note that the reported misfits for *GRIMM*, *xCHAOS* and *MF6* refer to predictions from these models (which were derived from other data sets) transformed to a 23 042 node STT-grid and compared to the *xCHAOS-corr-sub* data set.

5 DISCUSSION

5.1 Quadratic regularization versus entropy regularization

The 'quadratic' and 'entropy' models obtained in the synthetic trials in the presence of noise contamination appear rather similar at first glance—see Fig. 2, but careful examination of the correlation coefficients in the Table 4 and the recovered amplitudes reveals that entropy regularization (with $w = 10$ nT) performs slightly better at retrieving the full ($L = 140$) synthetic truth than conventional quadratic regularization. It appears that the difference between entropy and quadratic regularization is less extreme in the crustal field problem than in the core field problem (Jackson *et al.* 2007a) because the core field problem involves a more severe deconvolution problem due to the larger distance between the sources and the observations. How much better the entropy method does also depends on the choice of the default parameter w. If one is interested in reconstructing the full synthetic 'truth' including small scales as closely as possible, a choice of default parameter $w = 10$ nT performs best; on the other hand if one only wishes to reconstruct the larger scales (for example, up to $L = 60$) then a higher choice of $w = 50$ nT (closer to quadratic regularization) is better suited. A general problem with the maximum entropy method is that one requires prior knowledge of the field of interest in order to choose the default parameter (Skilling 1998; Maisinger *et al.* 2004).

The retrieved synthetic images in the experiments involving noisy data (for both choices of regularization) were somewhat disappointing with only the largest scale details of the reference 'truth' recovered. This was a consequence of the large amplitude of the noise that was added, which turned out to be more than that present in the real data. The high levels of noise necessitated rather heavy regularization which prevented the small scales from being imaged. Note however that stable images free from spurious structures were obtained using the STT-regularized method even at auroral latitudes where the amplitude of the imposed noise was largest. These synthetic tests illustrate that when attempting to image the small scale crustal field it is the quality of the observations rather than the imaging technique that is often the limiting factor.

© 2009 The Authors, *GJI*, **179,** 929–944
Journal compilation © 2009 RAS

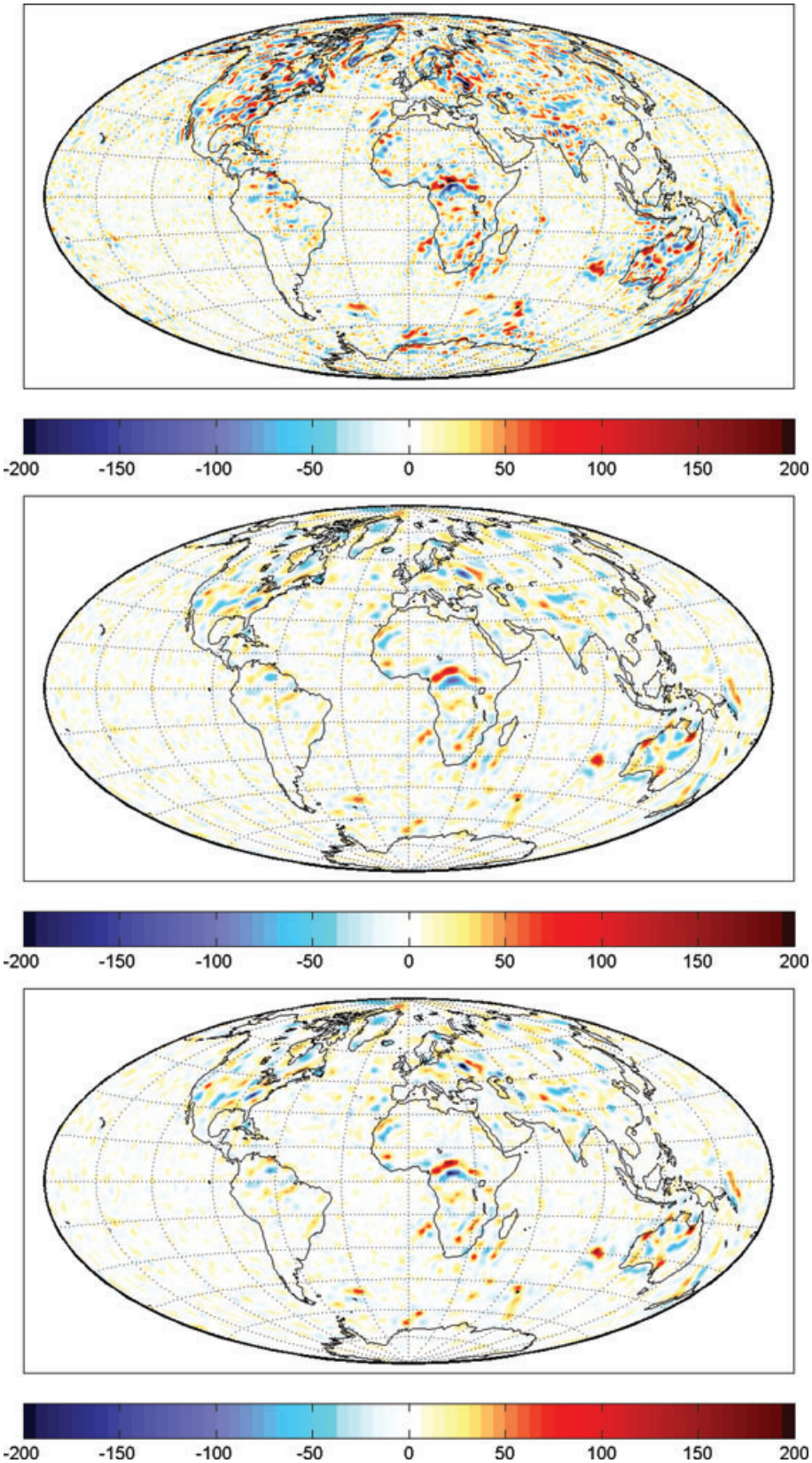

Figure 2. Radial magnetic field B_r at Earth's surface (in units of nT) for the true ($L = 140$) reference model (top panel) the quadratic regularized model (middle panel) and entropy regularized (bottom panel) with default parameter $w = 10$ nT, derived from the synthetic data set *xCHAOS-SYN-HMN*. Both inverted models were constructed using a damping parameter of $\lambda = 1 \times 10^{-3}$ (nT)$^{-2}$ (Hammer-Aitoff projection).

© 2009 The Authors, *GJI*, **179,** 929–944
Journal compilation © 2009 RAS

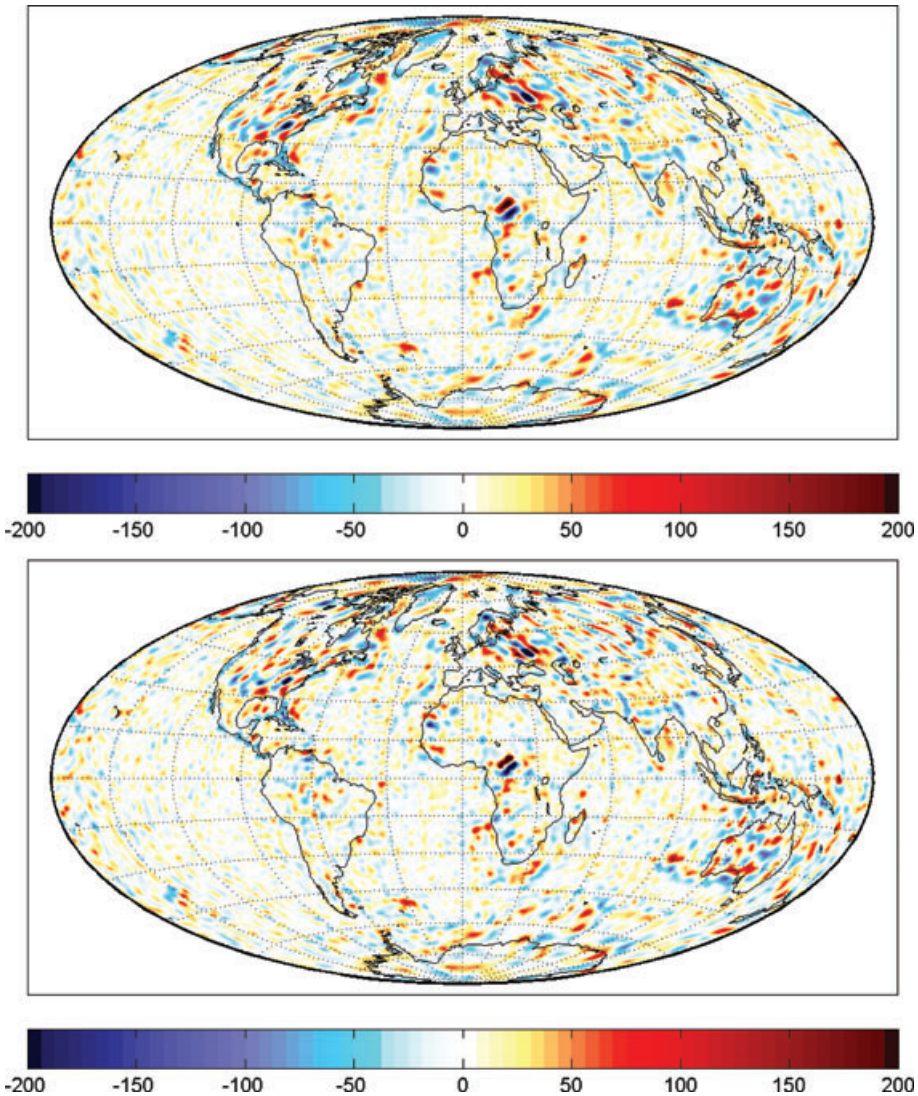

Figure 3. Radial magnetic field B_r at Earth's surface (in units of nT) for the quadratic regularized model *STT-CRUST-Q* (top panel) and entropy regularized model *STT-CRUST-E* with default parameter $w = 10$ nT (bottom panel). These models were derived from the real data set *xCHAOS-corr-sub* with a damping parameter of $\lambda = 2.5 \times 10^{-4}$ (nT)$^{-2}$ (Hammer-Aitoff projection). [Correction made after online publication 14 September 2009: the lower panel of Fig. 3 has been replaced.]

5.2 STT-CRUST field models from real data: comparison with previous models

The models *STT-CRUST-Q* and *STT-CRUST-E* we constructed from the real data are very similar as shown by their correlation coefficient of 0.960 reported in Table 5. [Correction made after online publication 14 September 2009: in the preceding sentence, the value '0.941' has been changed to '0.960'.] The quadratic model *STT-CRUST-Q* represents a rather conventional solution containing the minimum squared radial field required by the observations. It probably under-estimates the flux associated with some intense field features and also likely smoothes out some genuine small scale features. The entropy regularized model *STT-CRUST-E* might give a slightly more faithful image of Earth's crustal field, since high amplitude structures are not penalized during its construction. It possesses higher amplitude flux features and sharper boundaries in the field morphology.

Comparing global maps of the radial magnetic field at Earth's surface from *STT-CRUST-Q* and *STT-CRUST-E* in Fig. 3 with *GRIMM* (to degree 45) and *MF6* (to degree 120) in Fig. 4 it should first be noted that the STT models agree well with what is robustly known (as represented in the plot of the *GRIMM* model) concerning the structure of the large scale crustal field. This is true even in oceanic regions of low field amplitude and at polar latitudes, despite the use of very different data selection criteria and numbers of data. On the other hand, compared to the *MF6* model the STT models contain much less energy and sparser structures with differences most striking at the mid-to-high latitudes where the auroral electrojet currents contaminate the magnetic signal and crustal field estimation is difficult. Large differences are also obvious close to high amplitude continental anomalies, especially in eastern Europe, central Africa and Australia. This is apparently because in these regions our models contain sparser structures, with magnetic field energy more localized, although sometimes *MF6* also has significantly larger field amplitudes. Though our models certainly do not capture as much small scale detail as *MF6*, we are confident that those features present in the STT images are required to fit the *xCHAOS-corr-sub* data set. However, we are also aware that our

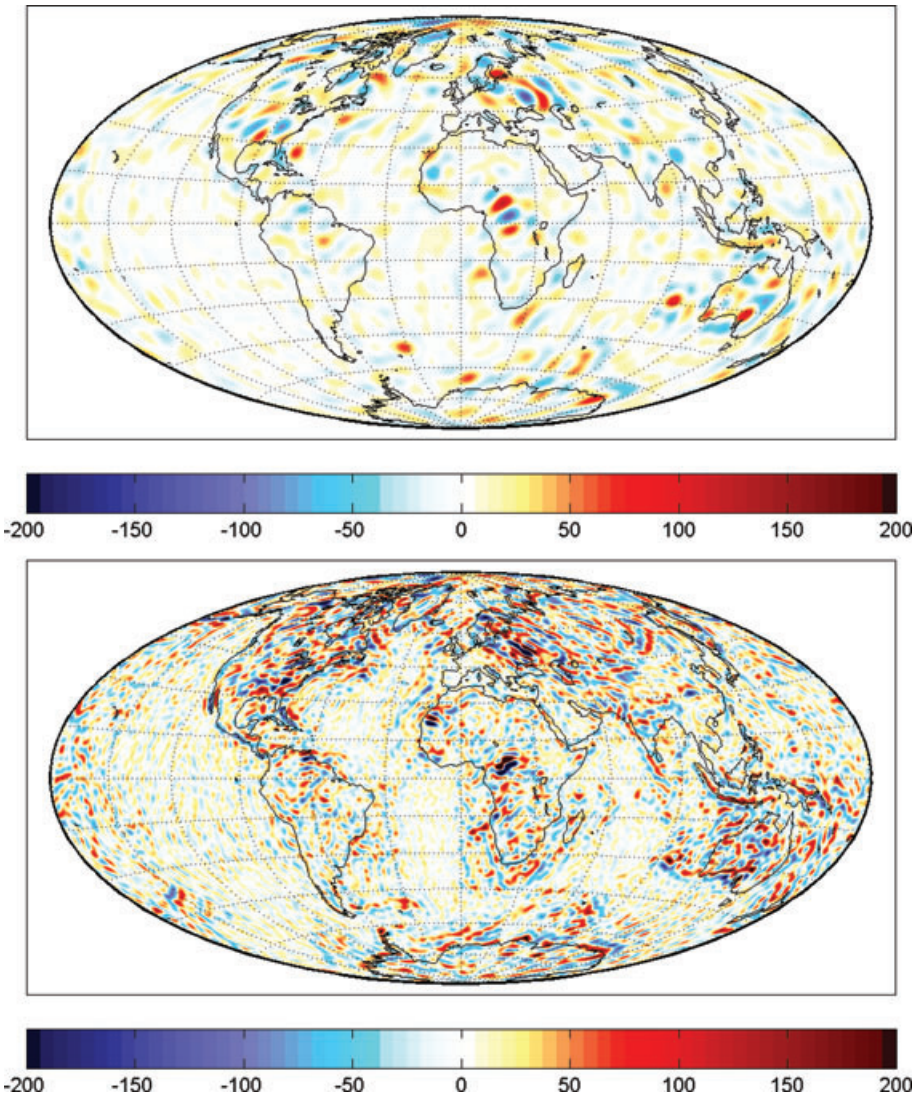

Figure 4. Radial magnetic field B_r at Earth's surface (in units of nT) from the *GRIMM* model of Lesur *et al.* (2008) for spherical harmonic degree 15–45 (top panel) and from the *MF6* model of Maus *et al.* (2008) for degree 16–120 (bottom panel) (Hammer-Aitoff projection).

models contain a small number of anomalous features possibly due to along track noise that remains in the *xCHAOS-corr-sub* data set which seems to require some further processing. In the future, using new improved data sets or data sets better optimized for studying small scale crustal fields, we expect the STT-regularized modelling method to will continue to perform well and to robustly image even smaller scale structures.

Quantitative comparisons between spherical harmonic crustal field models are often carried out on the basis of Lowes spectra and calculation of the spherical harmonic degree correlation. This is undoubtedly a valuable diagnostic approach, so we transformed our STT models to the spherical harmonic domain to permit such a comparison—the results for the power spectrum and the degree correlation are presented in Figs 5 and 6, respectively. The STT models agree rather well with *MF6*, *GRIMM* and *xCHAOS* up to degree 40; thereafter the STT models have lower power, though STT-CRUST-E has slightly higher power than *STT-CRUST-Q*. This is to be expected because the *STT-CRUST* models are minimum norm models, that is, they possess the minimum complexity required to fit the data while *MF6*, *GRIMM* and *xCHAOS* are constructed using least-square or least-absolute deviation fits to the observations and model truncation. The degree correlation of the STT models with the *xCHAOS* model is higher (over 0.9 for all degrees up to $L = 50$), than with the other two models. That is likely because our real data set is a subset of the data set used to build the *xCHAOS* model and because *xCHAOS* itself was used in the data selection procedure. The degree correlation of the STT models with *GRIMM* and *MF6* was also good up to degree 45. The correlation with *MF6* falls away rapidly beyond degree 55 at which point the regularization begins to strongly control the form of the STT solutions as also seen in their Lowes spectra which begin to decay around this degree. Although these results are interesting, we wish to point out again that transforming from a STT grid to spherical harmonics is not an exact procedure and results in some loss of power making precise comparisons in the spherical harmonic domain problematic.

The local comparison for North America between *STT-CRUST-E*, *GRIMM* and *MF6* presented in Fig. 7 nicely summarises how our STT models are intermediate in complexity between *GRIMM* and *MF6*. Again, the *STT-CRUST-E* model captures the same large scale structures as *GRIMM*, but also shows higher amplitudes

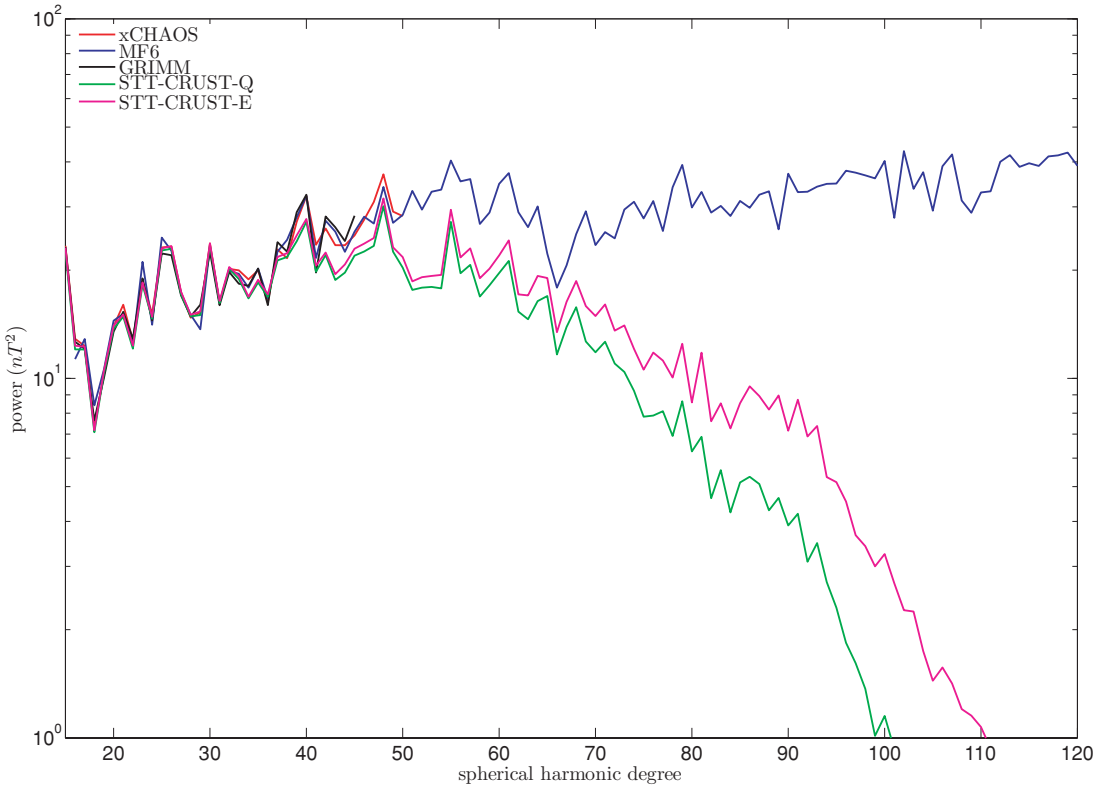

Figure 5. Lowes spectrum showing power (variance) per degree of the *xCHAOS* model (red line), the *MF6* model (blue line), the *GRIMM* model (black line), the *STT-CRUST-Q* model (green line) and the *STT-CRUST-E* model (violet line). [Correction made after online publication 14 September 2009: Fig. 5 has been replaced.]

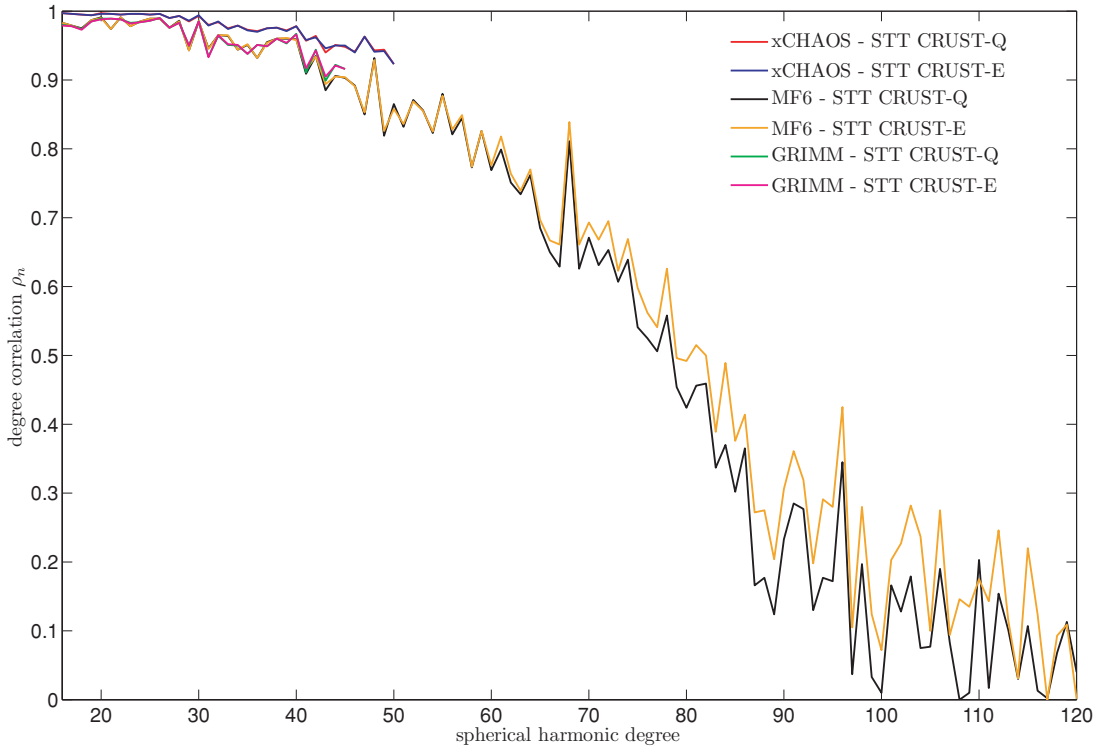

Figure 6. Degree correlation between the *xCHAOS* model, the *MF6* model, the *GRIMM* model and the *STT-CRUST-Q* and *STT-CRUST-E* models. [Correction made after online publication 14 September 2009: Fig. 6 has been replaced.]

© 2009 The Authors, *GJI*, **179,** 929–944
Journal compilation © 2009 RAS

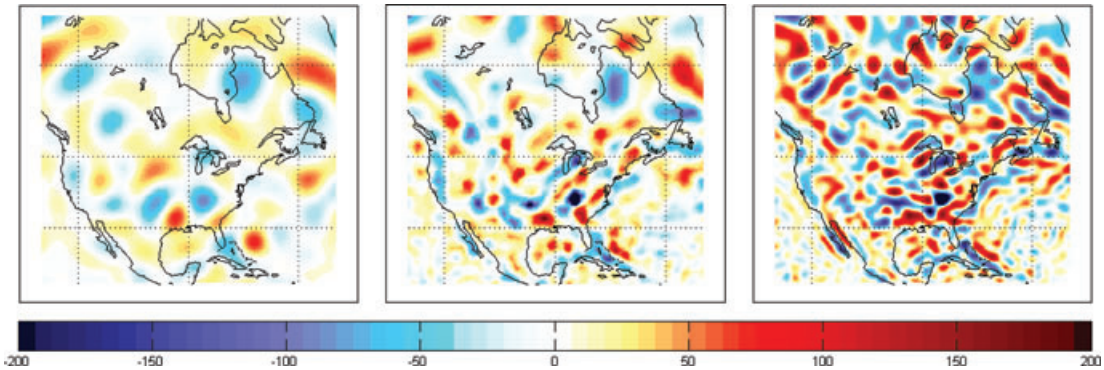

Figure 7. North America regional map of radial magnetic field B_r at Earth's surface (in units of nT) from the *STT-CRUST-E* model (middle panel), the *GRIMM* model of Lesur *et al.* (2008) (left-hand panel) and the *MF6* model of Maus *et al.* (2008) (right-hand panel) (Mercator projection). [Correction made after online publication 14 September 2009: Fig. 7 has been replaced.]

Table 5. Statistics of the models retrieved from the real data set *xCHAOS-corr-sub*.

Model	λ (nT)$^{-2}$	w (nT)	σ_{B_r} (nT)	min(B_r) (nT)	max(B_r) (nT)	misfit (L_1)	ρ
STT-CRUST-Q	0.00025	–	26.011	−370.384	292.306	0.884	0.960
STT-CRUST-E	0.00025	10.0	27.950	−629.045	607.050	0.883	1.000
GRIMM ($L = 45$)	–	–	20.123	−135.500	125.848	0.920*	0.554*
xCHAOS ($L = 50$)	–	–	22.812	−159.571	170.435	0.908*	0.624*
MF6 ($L = 120$)	–	–	40.973	−927.931	571.577	0.953*	0.602*

Notes: λ is the preferred damping parameter and w the chosen default value. σ_{B_r} is the rms value of the B_r field amplitudes. Min and max are the minimum and maximum field values, respectively. Misfit (L_1) stands for the L_1-norm measure of misfit of the model to the data normalized by the estimated errors, while ρ gives the correlation coefficient between *STT-CRUST-E* and the other models. The misfits and correlation coefficient marked with * are calculated after the original spherical harmonic models are transformed to a 23 042 node STT-grid.
[Correction made after online publication 14 September 2009: values in Table 5 have been corrected.]

and finer details of the geologically interesting structures such as the linear anomaly associated with the Baja California peninsula. Furthermore, Fig. 7 shows how many of the smaller scale structures present in *STT-CRUST-E* can also be identified in *MF6*, though *MF6* also contains much greater structure especially at high latitudes where the resolving ability of the STT models presented here was limited by the assignment of cautious error estimates. We believe the STT-crust models presented here are of interest because they are stable at Earth's surface, have not been arbitrarily truncated, and contain some sharp, localized structures.

In the future, with higher quality data and better external field models becoming available, workers should be able to construct crustal field images with lower values of the damping parameter λ, enabling small scale structures to be reliably imaged with both the quadratic and entropy regularization techniques. Such models may require finer grids to ensure that the obtained images are still controlled by model regularization rather than choice of grid size; although further STT grid refinements are currently computationally challenging this will certainly not be a major restriction in the years ahead as computing power continues to improve. Furthermore, the local basis nature of the STT representation opens the door to the possibility of local variations in the level of grid refinement, so for example, higher resolution grids could be constructed in regions where the data quality and spacing justify a more complex model. Development of the STT interpolation scheme from linear to higher order is also in principle a possibility that could be explored in future work. Finally, we note that the forward scheme is sufficiently flexible that magnetic field spatial gradient observations can easily be predicted and thus utilized in the inversion procedure; this is likely to be important when using data from future constellations of magnetic satellites.

6 CONCLUSIONS

New images of the crustal magnetic field at Earth's surface have been successfully constructed by inverting CHAMP, Ørsted and SAC-C satellite observations for a STT model consisting of local parameters. An absolute deviation measure of misfit was employed that is more robust to the presence of outliers than the conventional least squares approach. The resulting models possess comparable resolution to other recent spherical harmonic models derived from similar satellite data sets. Good agreement of the large scale structures with the *GRIMM* model was found, while the stable smaller scale structures imaged were often compatible with features present in the *MF6* model.

The STT crustal field models are able to satisfactorily account for the (noise contaminated) satellite observations whilst minimizing a global measure of field complexity. The later regularization procedure ensures the models are by construction stable at Earth's surface. Using a quadratic measure of field complexity and picking a model close to the knee of the misfit-norm trade-off curve was found to be a reliable procedure for producing satisfactory images of the crustal field at Earth's surface; the model *STT-CRUST-Q* was constructed in this manner. Using an entropy measure of field complexity with a default parameter of $w = 10$ nT resulted in the model *STT-CRUST-E*. This model is structurally sparse with sharp, well-localized features: regional comparisons of it with previous models (see Fig. 7) demonstrate the merits of the regularized STT approach.

The method of crustal field imaging presented here is a useful alternative to more conventional spherical harmonic schemes. Its local nature may become an even greater advantage when data accuracy and resolution improve, as is anticipated with upcoming multisatellite missions.

ACKNOWLEDGMENTS

We thank Nils Olsen for making the *xCHAOS* model as well as the CHAMP, Ørsted and SAC-C data used to construct it available, and also Nicolas Gillet for helpful discussions regarding the implementation of maximum entropy regularization. We also wish to thank Erwan Thébault and an anonymous reviewer for their detailed comments that helped us to improve the manuscript.

REFERENCES

Amirbekyan, A., Michel, V. & Simons, F.J., 2008. Parameterizing surface wave tomography models with harmonic spherical splines, *Geophys. J. int.,* **174,** 617–628.

Arkani-Hamed, J., Langel, R.A. & Purucker, M., 1994. Scalar magnetic anomaly maps of Earth derived from POGO and Magsat data, *J. geophys. Res.,* **99,** 24 075–24 090.

Aster, R., Borchers, B. & Thurber, C., 2005. *Parameter Estimation and Inverse Problems*, Elsevier Academic Press, Amsterdam.

Baumgardner, J.R. & Frederickson, P.O., 1985. Icosahedral discretization of the two-sphere, *SIAM J. Numer. Anal.,* **22**(6), 1107–1115.

Blakely, R.J., 1995. *Potential Theory in Gravity & Magnetic Applications*, Cambridge Univ. Press, Cambridge, UK.

Buck, B. & Maculay, V., 1991. *Maximum Entropy in Action*, Oxford Univ. Press, Oxford.

Cain, J.C., Wang, Z., Kluth, C. & Schmitz, D.R., 1989. Derivation of a geomagnetic model to $n = 63$, *Geophys. J. Int.,* **97,** 431–441.

Claerbout, J.F. & Muir, F., 1971. Robust modelling with erratic data, *Geophysics,* **38,** 826–844.

Cohen, Y. & Achache, J., 1990. New global vector magnetic anomaly maps derived from Magsat data, *J. geophys. Res.,* **95,** 1 0783–10 800.

Constable, C.G., Parker, R.L. & Stark, P.B., 1993. Geomagnetic field models incorporating frozen-flux constraints, *Geophys. J. Int.,* **113,** 419–433.

Covington, J., 1993. Improvement of equivalent source inversion technique with a more symmetric dipole distribution, *Phys. Earth planet. Int.,* **76,** 199–208.

De Santis, A., Torta, J.H. & Lowes, F.J., 1999. Spherical cap harmonics revisted and their relationship to ordinary spherical harmonics, *Phys. Chem. Earth.,* **24,** 935–941.

Farquharson, C.G. & Oldenburg, D.W., 1998. Non-linear inversion using general measures of data misfit and model structure, *Geophys. J. Int.,* **134,** 213–227.

Freeden, W. & Schreiner, M., 2009. *Spherical Functions of Mathematical Geosciences. A Scalar, Vectorial, and Tensorial Setup*, Springer, Heidelberg.

Freeden, W., Gervens, T. & Schreiner, M., 1998. *Constructive Approximation on the Sphere*, Clarendon Press, Oxford, UK.

Gillet, N., Jackson, A. & Finlay, C.C., 2007. Maximum entropy regularization of time-dependent geomagnetic field models, *Geophys. J. Int.,* **171,** 1005–1016.

Gubbins, D., 1983. Geomagnetic field analysis—I. Stochastic inversion, *Geophys. J. R. astr. Soc,* **73,** 641–652.

Gubbins, D., 2004. *Time Series Analysis and Inverse Theory for Geophysicists*, Cambridge Univ. Press, Cambridge, UK.

Gubbins, D. & Bloxham, J., 1985. Geomagnetic field analysis—III. Magnetic fields on the core-mantle boundary, *Geophys. J. R. astr. Soc,* **80,** 695–713.

Gubbins, D. & Roberts, N., 1983. Use of the frozen flux approximation in the interpretation of archaeomagnetic and palaeomagnetic data, *Geophys. J. R. astr. Soc,* **73,** 675–687.

Gull, S.F. & Daniell, G.J., 1978. Image reconstruction from incomplete and noisy data, *Nature,* **272,** 686–690.

Gull, S.F. & Skilling, J., 1984. Maximum entropy method in image processing, *IEE Proc. F Radar Signal Proc.,* **131,** 646–659.

Gull, S.F. & Skilling, J., 1990. The MEMSYS5 User's Manual, Maximum Entropy Data Consultants Ltd, Royston.

Haines, G.V., 1985. Spherical cap harmonic analysis, *J. geophys. Res.,* **90,** 2583–2591.

Hansen, P.C., 1998. *Rank-Deficient and Discrete Ill-Posed Problems: Numerical Aspects of Linear Inversion*, SIAM Monographs.

Hemant, K. & Maus, S., 2005. Geological modeling of the new CHAMP magnetic anomaly maps using a geographical information system technique, *J. geophys. Res.,* **110,** B12103, doi:10.1029/2005JB003837.

Hobson, M.P. & Lasenby, A.N., 1998. The entropic prior for distributions with positive and negative values, *Mon. Not. R. astr. Soc.,* **298,** 905–908.

Jackson, A., Constable, C. & Gillet, N., 2007a. Maximum entropy regularization of the geomagnetic core field inverse problem, *Geophys. J. Int.,* **171,** 995–1004.

Jackson, A., Constable, C.G., Walker, M.R. & Parker, R.L., 2007b. Models of Earth's main magnetic field incorporating flux and radial vorticity constraints, *Geophys. J. Int.,* **171,** 133–144.

Jaynes, E.T., 1957. Information theory and statistical mechanics, *Phys. Rev. Lett.,* **106**(4), 620–630.

Kellogg, O.D., 1954. *Foundations of Potential Theory*, Dover Publications, New York.

Korhonen, J.V. *et al.*, 2007. *Magnetic Anomaly Map of the World/Carte des anomalies magntiques du monde, 1st Edition, 1:50,000,000*, Commission of the Geological Map of the World (CCGM/CCGMW), UNESCO; ISBN 978-952-217-000-2.

Langel, R.A. & Hinze, W.J., 1998. *The Magnetic Field of the Earth's lithosphere, the Satellite Perspective*, Cambridge Univ. Press, Cambridge, UK.

Langel, R.A. & Whaler, K.A., 1996. Maps of the magnetic anomaly field at Earth's surface from scalar satellite data, *Geophys. Res. Lett.,* **23**(1), 41–44.

Langel, R.A., Sabaka, T.J., Baldwin, R.T. & Conrad, J.A., 1996. The near-Earth magnetic field from magnetospheric and quiet-day ionospheric sources and how it is modeled., *Phys. Earth. planet. Inter.,* **98,** 235–267.

Langlais, B., Purucker, M.E. & Mandea, M., 2004. Crustal magnetic field of Mars, *J. geophys. Res,* **109,** doi:10.1029/2003JE002048.

Lesur, V., 2006. Introducing localized constraints in global geomagnetic field modelling, *Earth Planets Space,* **58,** 477–483.

Lesur, V. & Maus, S., 2006. A global lithospheric magnetic field model with reduced noise level in the polar regions, *Geophys. Res. Lett.,* **33,** L13304, doi:10.1029/2006GL025826.

Lesur, V., Wardinski, I., Rother, M. & Mandea, M., 2008. GRIMM: the GFZ reference internal magnetic model based on vector satellite and observatory data, *Geophys. J. Int.,* **173,** 382–394.

Lowes, F.J., 1974. Spatial power spectrum of the main geomagnetic field, and extrapolation to the core, *Geophys. J. R. astr. Soc.,* **36,** 717–730.

Luenberger, D.G., 1969. *Optimization by Vector Space Methods*, John Wiley & Sons, Inc., New York.

Maisinger, K., Hobson, M.P. & Lasenby, A.N., 2004. Maximum-entropy image reconstruction using wavelets, *Mon. Not. R. astr. Soc.,* **347,** 339–354.

Maus, S., 2006. NGDC-720 model, http://www.ngdc.noaa.gov/geomag/EMM/emm.shtml.

Maus, S., Rother, M., Holme, R., Lühr, H., Olsen, N. & Haak, V., 2002. First scalar magnetic anomaly map from CHAMP satellite data indicates weak lithospheric field, *Geophys. Res. Lett.,* **29**(14), doi:10.1029/2001GL013685.

Maus, S., Lühr, H. & Purucker, M.G., 2006a. Simulation of the high-degree lithospheric field recovery for the *swarm* constellation of satellites, *Earth Planets Space,* **58,** 397–407.

Maus, S., Rother, M., Hemant, K., Stolle, C., Lühr, H., Kuvshinov, A. & Olsen, N., 2006b. Earth's lithospheric magnetic field determined to spherical harmonic degree 90 from CHAMP satellite measurements, *Geophys. J. Int.,* **164,** 319–330.

© 2009 The Authors, *GJI*, **179,** 929–944
Journal compilation © 2009 RAS

Maus, S., Sazonova, T., Hemant, K., Fairhead, J.D. & Ravat, D., 2007a. National geophysical data center candidate for the world digital magnetic anomaly map, *Geochem., Geophys., Geosyst. G*^{3}, **8**(6), Q06017, doi:10.1029/2007GC001643.

Maus, S., Lühr, H., Rother, M., Hemant, K., Balasis, G., Ritter, P. & Stolle, C., 2007b. Fifth-generation lithospheric magnetic field model from CHAMP satellite measurements, *Geochem., Geophys., Geosyst. G*^{3}, **8**(5), Q05013, doi:10.1029/2006GC001521.

Maus, S., Yin, F., Lühr, H., Manoj, C., Rother, M., Rauberg, J., Michaelis, I., Stolle, C. & Müller, R.D., 2008. Resolution of direction of oceanic magnetic lineations by the sixth-generation lithospheric magnetic field model from CHAMP satellite magnetic measurements, *Geochem., Geophys., Geosyst. G*^{3}, **9**(7), Q07021, doi:10.1029/2008GC001949.

Mayer, C. & Meier, T., 2006. Separating inner and outer earth's magnetic field from CHAMP satellite measurements by means of vector scaling functions and wavelets, *Geophys. J. Int.,* **167,** 1188–1203.

Mayhew, M., 1979. Inversion of satellite magnetic anomaly data, *J. Geophys.,* **45,** 119–128.

O'Brien, M.S. & Parker, R.L., 1994. Regularized geomagnetic field modelling using monopoles, *Geophys. J. Int.,* **118,** 566–578.

Olsen, N., 2002. A model of the geomagnetic main field and its secular variation for epoch 2000 estimated. from Ørsted data, *Geophys. J. Int.,* **149,** 454–462.

Olsen, N. & Mandea, M., 2008. Rapidly changing flows in the Earth's core, *Nat. Geosci.,* **1,** 390–394.

Olsen, N., Lühr, H., Sabaka, T.J., Mandea, M., Rother, M., Tøffner-Clausen, L. & Choi, S., 2006a. CHAOS—a model of the Earth's magnetic field derived from CHAMP, ørsted, and SAC-C magnetic satellite data, *Geophys. J. Int.,* **160,** 79–88.

Olsen, N. et al., 2006b. The *Swarm* end-to-end mission simulator study: a demonstration of separating the various contributions to Earth's magnetic field using synthetic data, *Earth Planets Space,* **58,** 359–370.

Parker, R.L., 1994. *Geophysical Inverse Theory*, Princeton Univ. Press, Princeton, NJ.

Parker, R.L. & Shure, L., 1982. Efficient modelling of Earth's magnetic field with harmonic splines, *Geophys. Res. Lett.,* **9,** 812–815.

Purucker, M.E., 2008. A global model of the internal magnetic field of the Moon based on Lunar prospector magnetometer observations, *Icarus,* **197,** 19–23.

Purucker, M.E. & Whaler, K.A., 2007. Crustal magnetization, *Treatise Geophys.,* **5,** 195–235.

Purucker, M.E., Sabaka, T.J. & Langel, R.A., 1996. Conjugate gradient analysis: a new tool for studying satellite magnetic data sets, *Geophys. Res. Lett.,* **23,** 1507–1510.

Ravat, D., Langel, R.A., Purucker, M.E., Arkani-Hamed, J. & Alsdorf, D.E., 1995. Global vector and scalar Magsat magnetic anomaly maps., *J. geophys. Res.,* **100,** 20 111–20 136.

Regan, R.R., Cain, J.C. & Davis, W.M., 1975. A global magnetic anomaly map, *J. geophys. Res.,* **80,** 794–802.

Rice, J.A., 1995. *Mathematical Statistics and Data Analysis*, Duxbury Press, Belmont, CA.

Sabaka, T.J., Olsen, N. & Langel, R.A., 2002. A comprehensive model of the quiet-time, near-Earth magnetic field: phase 3, *Geophys. J. Int.,* **151,** 32–68.

Sabaka, T.J., Olsen, N. & Purucker, M., 2004. Extending comprehensive models of the Earth's magnetic field with Ørsted and CHAMP data, *Geophys. J. Int.,* **159,** 521–547.

Scales, J.A., Gersztenkorn, A. & Treitel, S., 1998. Fast l_p solution of large, sparse, linear systems: application to seismic travel time tomography, *J. Comp. Phys.,* **75,** 314–333.

Shannon, C.E., 1948. A mathematical theory of communication, *Bell Syst. Tech. J.,* **27,** 379–423.

Shure, L., Parker, R.L. & Backus, G.E., 1982. Harmonic splines for geomagnetic modelling, *Phys. Earth planet. Inter.,* **28**(3), 215–229.

Simons, F.J. & Dahlen, F.A., 2006. Spherical slepian functions and the polar gap in geodesy, *Geophys. J. Int.,* **166,** 1039–1061.

Simons, F.J., Dahlen, F.A. & Wieczorek, M.A., 2006. Spatiospectral localization on a sphere, *SIAM Rev.,* **48,** 504–536.

Sivia, D.S. & Skilling, J., 2006. *Data Analysis: A Bayesian Tutorial*, Oxford Univ. Press, Oxford.

Skilling, J., 1988. The axioms of maximum entropy, *In Maximum Entropy and Bayesian Methods on Science and Engineering,*Vol. 1, pp. 173–187.

Skilling, J., 1998. Massive inference and maximum entropy, in *Maximum Entropy and Bayesian Methods on Science and Engineering*, pp. 1–14.

Tarantola, A., 2005. *Inverse Problem Theory and Methods for Model Parameter Estimation*, SIAM, Society for Industrial and Applied Mathematics, Philadelphia.

Thébault, E., 2006. Global lithospheric magnetic field modelling by successive regional analysis, *Earth Planets Space,* **58,** 485–495.

Thébault, E., 2008. A proposal for regional modelling at the Earth's surface, R-SCHA2D, *Geophys. J. Int,* **174,** 118–134.

Thébault, E., Mandea, M. & Schott, J.J., 2006a. Modeling the lithospheric magnetic field over France by means of revised spherical cap harmonic analysis (R-SCHA), *J. geophys. Res.,* **111,** doi:10.1029/2005JB004110.

Thébault, E., Schott, J.J. & Mandea, M., 2006b. Revised spherical cap harmonic analysis (R-SCHA), *J. geophys. Res.,* **111,** doi:10.1029/2005JB003836.

Thébault, E., Hemant, K., Hulot, G. & Olsen, N., 2009. On the geographical distribution of induced time-varying crustal magnetic fields, *Geophys. Res. Lett.,* **36,** L01307, doi:10.1029/2008GL036416.

Thomson, A.W.P. & Lesur, V., 2007. An improved geomagnetic data selection algorithm for global geomagnetic field modelling, *Geophys. J. Int.,* **169,** 951–963.

Tikhonov, A.N. & Arsenin, V.Y., 1977. *Solution of Ill-Posed Problems*, Winston and Sons, Washington.

Walker, M.R. & Jackson, A., 2000. Robust modelling of the Earth's magnetic field, *Geophys. J. Int.,* **143,** 799–808.

Whaler, K.A., 1994. Downward continuation of Magsat lithospheric anomalies to Earth's surface, *Geophys. J. Int.,* **116,** 267–278.

Whaler, K.A. & Purucker, M.E., 2005. A spatially continuous magnetization model for Mars, *J. geophys. Res.,* **110,** doi:10.1029/2004JE002393.

© 2009 The Authors, *GJI*, **179,** 929–944
Journal compilation © 2009 RAS